1 **Evolution of microstructure in neutron irradiated cold rolled tungsten and its**
2 **correlation with hardness**
3
4 K. Mergia[1,*], V. Chatzikos[1,2], E. Manios[1], S. Dellis[1], D. Papadakis[1,3], D. Terentyev[4], G. Bonny[4],
5 A. Dubinko[4], I.E. Stamatelatos[1], S. Messoloras[1] and M. Rieth[5]
6
7 [1]Institute of Nuclear and Radiological Sciences and Technology, Energy and Safety, NCSR
8 Demokritos, Athens, 15310, Greece,
9 [2]Department of Physics, School of Sciences, University of Ioannina, Ioannina, 45110, Greece,
10 [3]Department of Physics, School of Sciences, University of Athens, Athens, 15772, Greece,
11 [4]SCK CEN, Nuclear Materials Science Institute, Boeretang 200, 2400 Mol, Belgium
12 [5]Karlsruhe Institute of Technology, Institute for Applied Materials, 76344 Eggenstein-
13 Leopoldshafen, Germany
14

15 **ABSTRACT**
16 The understanding of the neutron irradiation effects in tungsten is of significant importance for
17 its use as a plasma facing material in future fusion devices. In this study, cold rolled tungsten is
18 neutron irradiated at the Belgian BR2 fission reactor at the temperatures 600, 800, 900 and
19 1200 °C to a dose of 0.18 displacements per atom (dpa). The neutron induced changes in the
20 microstructure are investigated as a function of irradiation temperature using transmission
21 electron microscopy, positron annihilation spectroscopy and electrical resistivity
22 measurements. The influence of the irradiation on the elastic properties and the hardness is
23 examined using the impulse excitation techniques and depth-sensing indentation. Voids and
24 dislocation loops are observed at all the irradiation temperatures. As the irradiation
25 temperature increases the number density of both voids and loops decreases whereas their
26 size increases. The total dislocation density increases after irradiation at 600 °C whereas it
27 decreases for higher temperature irradiations. Furthermore, the formation of very small
28 vacancy clusters in the temperature range of 800 - 900 °C is revealed by PAS measurements. A
29 systematic decrease in the values of Young's and shear moduli is observed as the irradiation
30 temperature increases and this decrease is of about 3.5% after irradiation at 1200 °C. A
31 considerable hardening effect is observed at all irradiation temperatures. The hardness
32 increases with irradiation temperature reaching a maximum at 800 °C and remains almost
33 constant at higher irradiation temperatures.
34
35 **Keywords**: tungsten, neutron irradiation, transmission electron microscopy, positron
36 annihilation spectroscopy, mechanical properties, electrical resistivity

* Corresponding author: K. Mergia, kmergia@ipta.demokritos.gr

1 INTRODUCTION

The safe and prolonged operation of fusion reactors requires the use of plasma facing materials that can withstand high energy neutron irradiation, high heat fluxes, impact of highly energetic particles and cyclic stress loading [1]. Tungsten (W) is the prime choice for armor materials for the divertor and first wall in current and future fusion devices due to its attractive properties such as high melting point, high thermal conductivity, low tritium retention, good sputtering resistance, thermal stress and shock resistance and low swelling under irradiation [2, 3]. However, its brittle behavior at temperatures ranging from room temperature to several hundreds of degrees Celsius depending on the microstructure, limits its performance and therefore its potential for fusion applications. Several methods of microstructural modification have been proposed in order to improve the ductility and fracture toughness of tungsten. It has been shown that cold-rolling is a process which improves the ductility of W down to room temperature and at the same time results to a rather high strength material [4, 5].

In the literature there is a number of investigations regarding the microstructure and mechanical properties of tungsten and its alloys under fission neutron irradiation [6, 7, 8, 9, 10, 11, 12, 13, 14, 15, 16, 17, 18, 19, 20, 21, 22, 23, 24, 25, 26]. Neutron irradiation results in extensive damage in the material that is revealed in the form of vacancy clusters or voids and dislocation loops. In addition, transmutation reactions produce Re, Os and Ta which diffuse and form precipitates or clusters [25]. These three types of defect clusters, i.e. voids, dislocation loops and precipitates, can cause the increase of hardness and yield strength and decrease of tungsten's ductility. Dislocation loops prevail at temperatures below 500 °C [7, 13], whereas higher irradiation temperatures promote voids formation. Void lattice formation has been observed after irradiation at 550 °C to a fast neutron fluence of 10^{22} n/cm^2 [27]. It has been shown that the hardness and microstructure changes exhibit a clear dependence on the neutron energy spectrum [12].

In the current work we investigate the evolution of the microstructure of cold rolled tungsten irradiated at 0.18 dpa and in the temperature range from 600 to 1200 °C at the Belgian Material Test Reactor BR2. Open volume defects are determined by positron annihilation lifetime spectroscopy (PALS) and the irradiation induced changes in the microstructure by transmission electron microscopy (TEM). The impact of the irradiation induced microstructural changes on the elastic properties and hardness is assessed by impulse excitation technique and depth sensing instrumented indentation. In addition electrical resistivity measurements are employed to evaluate the microstructural evolution and the contribution of the radiation induced defects.

2 MATERIALS AND METHODS

2.1 Material and neutron irradiations

The tungsten material, with a purity of better than 99.97 wt%, was produced by PLANSEE SE in sheet form using a powder metallurgical route consisting of sintering and rolling [28]. The tungsten sintered compact is heated to a temperature of above 1250 °C ("hot-rolling") and is subsequently rolled to a plate thickness of 5.5 mm. Then this plate is "cold rolled" to a temperature of below 1000 °C and it is brought by progressive rolling steps to 1 mm thicknesses. The resulting material has a plate-like grain shape [28, 29]. Disks were sectioned from the plate using electrical discharge machining and were subsequently mechanically polished from both sides using diamond suspension up to 0.25 µm and colloidal silica at the final stage to obtain mirror quality surface and removing surface oxide and stresses/surface damage induced by the EDM cutting. The resulting thickness of the samples was about 0.5 mm.

Neutron irradiations were performed at the Belgian Material Test Reactor BR2. In order to maximize the fast-to-thermal neutron ratio and thus achieve transmutation rates of W into Re and Os closer to those expected under ITER and DEMO conditions, the irradiations were performed inside a fuel element and in the maximum fast neutron (> 0.1 MeV, 7×10^{14} n/cm^2/s) flux position.

The samples were encapsulated in stainless steel tube filled with helium. The thickness (1.5 mm) of the steel tube was adjusted to maximize the shielding from the thermal neutrons. The gap between the samples and the tube was adjusted to achieve 600, 800, 900 and 1200 °C following thermal and neutronic calculations. The irradiation channel was selected to comply as much as possible with the target neutron flux, which governs the irradiation temperature for the given capsule design. The typical temperature excursion within a cycle is about 5% (or less depending on the position of the capsule in the channel) of the target irradiation temperature. The uncertainty on the temperature calculation is about 5% arising from the uncertainties of the gap dimension and the nuclear heat release in tungsten.

The irradiation dose was 0.18 displacement per atom (dpa), which was calculated by MCNPX 2.7.0 based on the total fast neutron fluence (8.9×10^{20} n/cm^2, >0.1 MeV) achieved after three irradiation cycles of a total duration of 70 days [30]. The dpa cross sections for W have been prepared from the JENDL4 file (MT444) for the threshold displacement energy of 55 eV, following the recommendation of IAEA [31].

2.2 Transmission Electron Microscopy

TEM was performed with JEOL 3010 TEM operating at 300 kV. The TEM samples were prepared by cutting the irradiated disks into pieces with a size of about 1.5 × 1.5 × 0.5 mm and then the coupons were mechanically polished using SiC paper with grit sizes of 220, 500, 1200, 2000 and 4000 to achieve 70-100 µm thickness. The coupons were rinsed in ethanol and then

glued on 3 mm copper grids with an aperture of 1 mm. Finally, TEM specimens were polished electrochemically with a solution of 1.5 wt.% NaOH in water with applied voltage of 30 V. The local thickness of the specimen was determined from the convergent beam electron diffraction pattern. Several measurements in different areas were performed to make sure that the observed microstructure is indeed statistically representative. A typical thickness of the area under observation was 50-100 nm. The average dislocation density was measured following the methodology used in [32]. The overall methodology for the registration of tungsten microstructure was adopted from our earlier works where the same tungsten grades were investigated after plastic deformation and high flux plasma exposure [33,34,35,36].

2.3 Positron annihilation spectroscopy

2.3.1 Positron Annihilation Lifetime spectroscopy (PALS)

Positron annihilation lifetime measurements were carried out at room temperature using Ortec® PLS-system [37, 38]. The ^{22}Na radionuclide (from evaporated ^{22}NaCl metallic salt), encapsulated in 3.6 mg/cm^2 thin polymide (Kapton®) windows, was used as the positron source with an activity of 100 μCi. The active area of the source is 5 mm. The positron source was sandwiched between two pieces of identical specimens. The time resolution, i.e. the Full Width Half Maximum (FWHM) of the prompt spectrum, was measured with ^{60}Co and was found around 260 ps. The detectors were placed at a distance of about 5 mm from the sample. For each spectrum at least four million counts were collected. The mean penetration depth of positrons corresponding to the mean energy of the ^{22}Na spectrum is 11 μm, which is large enough to avoid any surface effects.

The data analysis was performed using LT10 software [39, 40]. The experimental spectra were fitted to the expression of the equation,

$$S(t) = B + R(t) \otimes (I_{src} + I_s) = B + R(t) \otimes \left(\sum_{k=1}^{L} I'_k e^{-\lambda_{src,k}t} + \sum_{i=0}^{N} I_i e^{-\lambda_i t} \right). \tag{1}$$

The components k of the I_{src} refer to air, kapton and source part of the spectrum. The sample response I_s consists of N components with $i = 0$ referring to the defect free material and $i = 1,...,N$ to the different open volume defects within the sample. Each component is characterized by the relevant intensity I_i and its lifetime $\tau_i = 1/\lambda_i$. $R(t)$ is the resolution function and B the background. In this expression it is assumed that in each defect the positron is annihilated independently of the other defects and the defect free matrix, i.e. there are no correlations.

The resolution function was described by a sum of two Gaussians and it was determined by ^{60}Co measurements. The I_{src} components (eq. 1) were determined by measurements of well annealed and of high purity (better than 99.99%) reference materials (Al, Co, Ni, Cd and Pb).

The lifetime value of the first source component, $\tau_{src,1}$, comprising the annihilations in the source itself and the surrounding Kapton® foil was found (371 ± 1) ps and it is in good agreement with values reported in the literature (in the range 368 - 386 ps for Kapton and NaCl source in [39, 41, 42], 385 ps for Kapton in [43]). The second source component, $\tau_{src,2}$, corresponding to the annihilations in the air between the source and the specimen, exhibits a lifetime value of (2.20 ± 0.03) ns and a small intensity of (2.0 ± 0.2) %.

2.3.2 Doppler broadening spectroscopy

The coincidence Doppler broadening (CDB) spectrum provides the momentum distribution of the electrons in the material. Low momentum is associated to valence/free electrons found near open volume defects. High momentum is associated to core electrons and it can be used to determine the chemical environment around a positron–electron annihilation site.

The CDB setup [44,45,18] consists of two movable high-purity Ge detectors (coaxial HPGe detector from Canberra type GC3018) with high-energy resolution (FWHM = 0.8 keV at 122 keV and FWHM = 1.8 keV at 1332 keV) and build-in preamplifier (model 2101P). Both the electronics as well as the hardware were optimized to measure highly active specimen with moderate detector dead time (< 20%) and very low background. The measurements were performed at room temperature using a [22]Na positron source.

The low and high-momentum regions in the CDB spectrum were quantified based on the S- and W-parameters, respectively. The S- and W-parameters were defined as the ratio of low momentum ($|c\,p_L| < 2.5 \times 10^{-3}\ m_0 c$) and high momentum ($15 \times 10^{-3}\ m_0 c < |c\,p_L| < 25 \times 10^{-3}\ m_0 c$) regions in the CDB spectrum to the total region, respectively. Here c denotes the lightspeed, m_0 the electron rest mass and p_L the longitudinal component of the positron-electron momentum along the direction of the γ-ray emission.

2.4 Electrical Resistivity

Electrical resistivity was measured employing the collinear 4-point probe (4PP) method using Keithley 2182A nanovoltmeter and Keithley 6221 AC and DC current source. The two outer pins of the 4PP are connected to the current source, while the two inner pins are connected to the nanovoltmeter. The nanovoltmeter in combination with the current source were configured to operate as a single device in the so called "Delta Mode", where the current source is supplying a DC current with alternating polarity (reversing at a frequency of 24 Hz) in order to eliminate the effects of the thermal electromotive force (emf). The measurements were performed at 20 ^{o}C and the current used was in the range 10-100 mA. The ratio of the measured voltage to the supplied current is the 4PP resistance which has to be multiplied by suitable geometric factors to give the resistivity of the sample [46, 47]. The geometric factor to account for the sample thickness was calculated by combining Maxwell's equations for static

1 fields with Ohm's law and the boundary conditions imposed by macroscopic geometric features
2 (such as sample thickness and pins' spacing). For the geometric factor to account for the finite
3 sample dimension laterally compared to the 4PP spacing the relation as described in [47] for
4 circular samples was used which depends on the ratio of the sample's diameter to the pins'
5 spacing.
6
7 **2.5   Elastic Properties**

8 The Young's modulus, E, the shear modulus, G, and the Poisson ratio, v, of the non-
9 irradiated and irradiated W samples were obtained employing Impulse Excitation Technique
10 (IET) [48] using the Buzz-o-Sonic system. For these tests, the disc shaped specimen was
11 supported by a foam material and excited by a light mechanical impulse. A microphone located
12 in the vicinity of the sample was used to transmit sound vibrations to the signal processing unit.
13 From the spectrum the first and second natural resonant frequencies, $f_{1,2}$, are obtained and
14 the Young's modulus according to ASTM E1876 [49] is given by
15

16
$$E = \frac{E_1 + E_2}{2}, \ E_{1,2} = \frac{3\pi d^4 f_{1,2}^2 \rho \left(1 - v^2\right)}{K_{1,2}^2 t^2} \tag{2}$$

17

18 where ρ is the density, t is the thickness and d is the diameter of the sample and $K_{1,2}$ are
19 geometric factors. The Poisson ratio is determined from ASTM E1876 tables given as a function
20 of the ratio of thickness versus radius of the sample and the frequencies. The shear modulus is
21 determined by the equation

22
$$G = \frac{E}{2\left(1 + v\right)} \tag{3}$$

23
24 **2.6   Vickers hardness**

25 Indentation measurements were carried out at room temperature employing NANOVEA's
26 mechanical tester and a Vickers indenter. The indentation direction was normal to the plane
27 defined by the rolling and transversal direction of the W sheet. The maximum load was set at 3
28 N, while the (un)loading rate was 20 N/min. A dwell time of 200 s was applied before starting of
29 the unloading process. The loading rate was selected after a series of preliminary indentation
30 tests to achieve stability in the hardness values. The holding time was chosen such as to attain
31 equilibrium conditions, i.e. almost no change of the indentation depth. A set of nine
32 indentation tests, spaced by 200 μm, were performed. An optical microscope was used to
33 select the indented area free from visible defects. The Vickers hardness, H_V, was calculated as

the ratio of the maximum applied force F_{max} and the actual pyramidal surface area, A, of the resulting indentation determined from the imprints using optical microscopy images as

$$H_V = \frac{F_{max}}{A} = \frac{2F_{max}}{d_{mean}^2}\sin(\alpha/2),\qquad(4)$$

where d_{mean} is the mean diagonal length measured from corner to corner on the residual impression in the specimen surface and $\alpha = 136°$ is the face angle of the square-based diamond pyramid of the Vickers indenter.

## 3 RESULTS AND DISCUSSION

3.1 Microstructure characterization

3.1.1 TEM

The microstructure of the reference (unirradiated) material is characterized by grains elongated along the rolling direction with sub-grain size in the range 1.5 – 2 µm, while it presents a dense tangled dislocation network with an average dislocation density of 1×10^{14} m^{-2} and low angle grain boundaries [29, 50]. Also, dislocation loops were observed with their size in the range of 3-11 nm and their density around 6.3×10^{19} m^{-3}.

At 600°C (Fig. 1a, 1d) the mean size of the voids is 1.15 nm (density is 1.25×10^{23} m^{-3}) and the mean loop size is around 3 nm (density is 2×10^{22} m^{-3}). The voids are distributed homogeneously (see Fig.1d), while the loop's spatial distribution depends on the presence/absence of dislocation lines. In the dislocation-free region (see Fig.1a) the loops form random arrays, while near the dislocation lines the loops decorate dislocation lines.

At 800°C the mean size of the voids (see Fig.1e) has slightly increased up to 1.8 nm and their density has slightly decreased down to 8.8×10^{22} m^{-3}. The formation of voids having a mean size of 3.8 nm and density 8×10^{21} m^{-3} has been observed in neutron irradiated pure tungsten after irradiation at 800 °C up to a dose of 0.98 dpa while after the irradiation at 500 °C no voids have been observed [11]. The same authors reported also the presence of dislocation loops with a mean size of 2.9 nm and density 3.3×10^{22} m^{-3} only at the lower irradiation temperature of 500 °C. The density of the loops has decreased by one order of magnitude, while the mean loop size decreased just slightly down to 2.66 nm. As in the case of 600 °C irradiation the spatial distribution of the loops has been found to depend on the particular area of observation being rich or depleted with dislocation lines, an example is shown in Fig.1b.

600 °C	800 °C	1200 °C
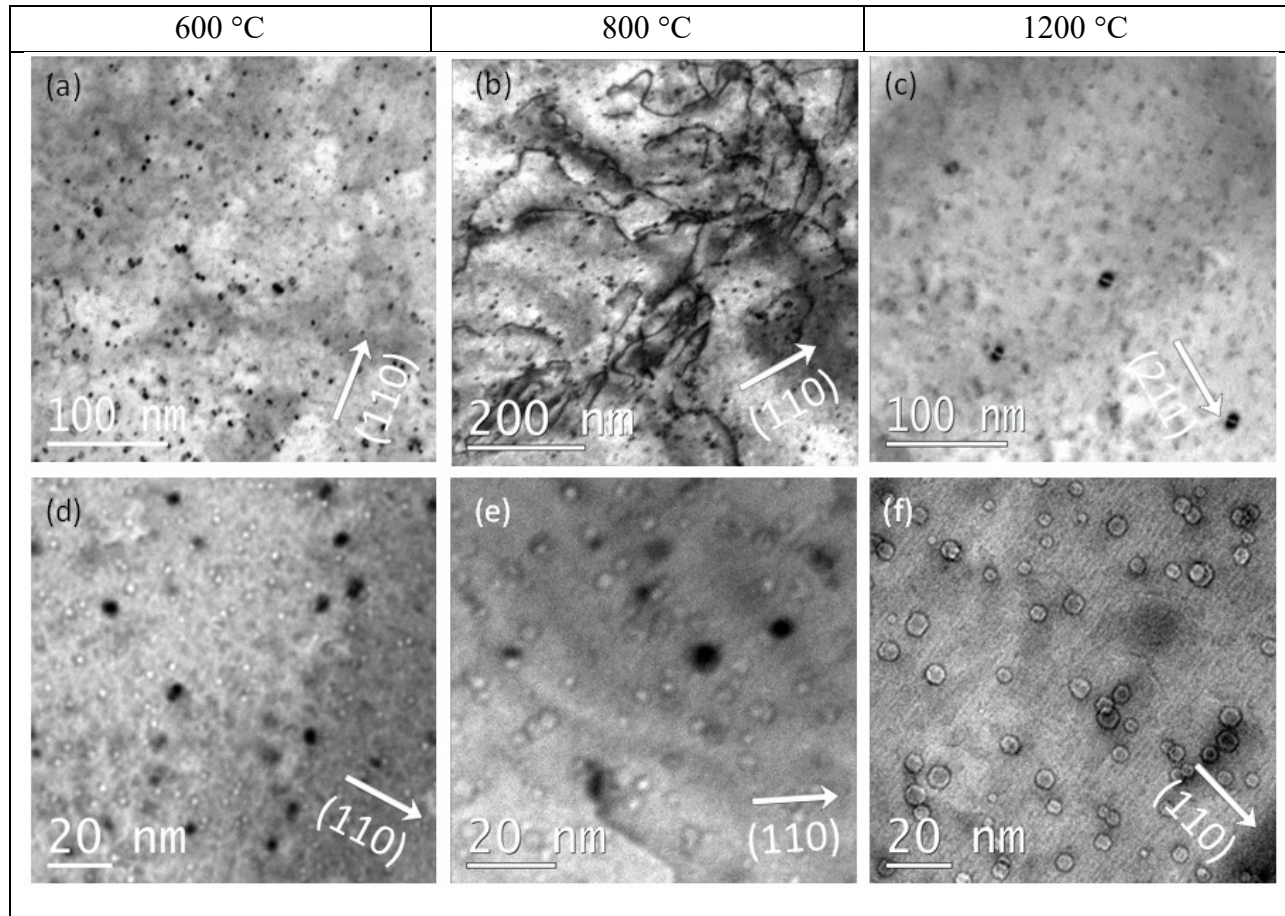
1 **Fig.1**. Bright field TEM images of the samples irradiated at (a,d) 600°C, (b,e) 800°C, (c,f) 1200°C.
2 (a) T_{irr}=600°C overview of the loops (black dots) in dislocation-free region; (b) T_{irr}=800°C
3 overview of the loops (black dots) and dislocation rich areas; (c) T_{irr}=1200°C overview of the
4 loops (black dots); (d) T_{irr}=600°C voids in under focus contrast, loops are black objects; (e)
5 T_{irr}=800°C voids in under focus contrast, loops are black objects; (f) T_{irr}=1200°C voids in under
6 focus contrast. The images were obtained with g[110] (a, b, d, e, f) and g[211] (c).

7

8   After irradiation at 1200°C the mean size of both the loops and the voids has been
9 increased. At the same time the density of the dislocation loops has decreased nearly by two
10 orders of magnitude compared to that at 600 °C. The mean loop size has increased by a factor
11 of three (from 1.15 nm at T_{irr}=600°C to 3.81 nm). The voids and the loops present a
12 homogeneous spatial distribution. The large voids have well pronounced faceted shapes as
13 shown in Fig.1f.
14   Table I summarizes TEM findings for the voids, loops and dislocation lines at the various
15 irradiation temperatures at the same neutron irradiation damage of 0.18 dpa. Detailed
16 information about the TEM investigation of the microstructure of the W sheet material of the
17 current study is presented elsewhere [50]. The values measured directly from TEM are: a) void
18 diameter, d_{void} , and their number density per unit volume, N_{void} , b) the diameter of loops,

d_{loop}, and their number per unit volume, N_{loop}, and c) the dislocation lines length per unit volume, N_{line}. The total dislocation density is calculated as a sum of dislocation lines density (N_{line}, Table 1) and the term $\pi d_{loop} \cdot N_{loop}$ corresponding to dislocations loops.

Table I. Radiation damage microstructural parameters obtained by TEM and I_1/I_0 ratio from PALS results.

	Voids			Loops		Dislocation lines	Total Dislocations	PALS
	Diameter	Density	Volume fraction	Diameter	Density	Density	Density	
T_{irr} (°C)	d_{void} (nm)	N_{void} (10^{23} m^{-3})	f_{void} (%)	d_{loop} (nm)	N_{loop} (10^{22} m^{-3})	N_{line} (10^{14} m^{-2})	N_t (10^{14} m^{-2})	I_1/I_0
Unirradiated	-	-		3-11	0.0063	1.0	1.02	1.012(8)
600	1.15	1.2	0.01	3	2.0	0.35	2.2	2.2(1)
800	1.83	0.88	0.028	2.66	0.317	0.308	0.57	0.60(2)
900								0.40(1)
1200	3.8	0.24	0.069	5.86	0.073	0.175	0.31	1.6(3)

Voids are not detected in the unirradiated material and irradiation results in their formation. Their volume increases with irradiation temperature, a four-fold increase is observed when the irradiation temperature is raised from 600 to 800^{0}C and a nine-fold increase when it is raised to 1200 °C. The volume fraction (in %) of the voids increases linearly with the irradiation temperature, T_{irr}, as

$$f_{void}(T) = f(600° \mathrm{C}) \cdots \cdots \cdots (T_{irr} \cdots \cdots °C) \cdots \cdots \cdots (T_{irr} \cdots \cdots °C). \quad (5)$$

Dislocation loops are very few in the unirradiated sample. Irradiation at 600 °C increases their number density by a factor of around 300. However, irradiation at 800 °C results to a loop number density around six times lower than that produced at 600 °C and irradiation at 1200 °C thirty times lower density compared to 600 °C irradiation. As in all the irradiation temperatures the same damage has been produced (0.18 dpa) and the irradiation time is also the same, we can conclude that the effects observed can be attributed solely to temperature. Therefore, higher temperature can cause either reduction of the irradiation induced loop generation or higher rate of annihilation of produced loops.
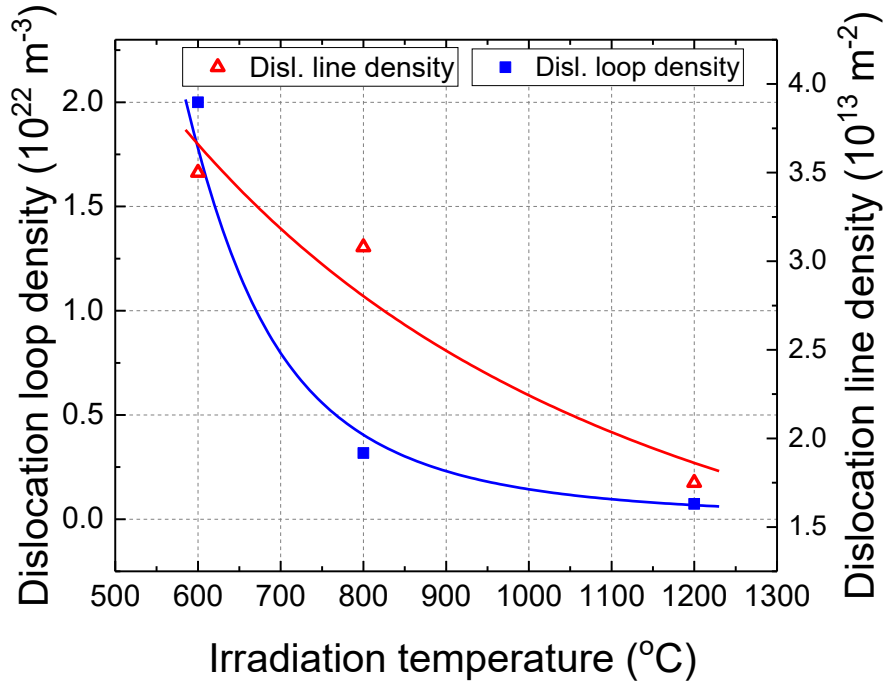
Fig. 2. Dislocation loop and line density as a function of irradiation temperature. The solid lines are least square fits of eq. (6) to the data.

The effect of irradiation temperature is also observed in the number of dislocation lines. An irradiation at 600 °C reduces the high line dislocation density of the unirradiated material by a factor of about three and irradiation at 1200 °C by a factor of about six. Therefore, the combined field of neutron irradiation (characterized by the fluence or damage in dpa) and temperature, T_{irr}, result in complex phenomena with respect to the generation/annihilation of both loop and line dislocations. These results may be summarized in a function of the number density of dislocations in the form

$$N\left(T_{irr},t\right) = N_0 \exp(-\frac{t}{\tau\left(T_{irr}\right)}) + a_{irr}\tau\left(T_{irr}\right)\left[1 - \exp(-\frac{t_{irr}}{\tau\left(T_{irr}\right)})\right], \qquad (6)$$

where N_0 is the dislocation density in the unirradiated sample, a_{irr} the number of dislocations generated by the irradiation per unit time per unit volume (assumed temperature independent), t_{irr} is the irradiation time and $\tau = \tau_0 \exp\left(E/k_B T_{irr}\right)$ the lifetime of the dislocations with E the activation energy and k_B the Boltzmann constant [51]. In Fig. 2 the fitted curves of dislocation densities for both loops and lines using eq. (6) are shown and the fitted parameters are presented in Table II. The determined energies are reasonably accurate (Arrhenius plot of asymptotic form of eq. (6)), whereas the other values are correct in the order of magnitude. We observe that irradiation results in the formation of dislocation loops and not

10

1 of dislocation lines. The dislocation lines pre-existing in the samples are annihilated and this is
2 due to the temperature and not to the irradiation, i.e. higher annihilation the higher the
3 temperature. The annihilation of dislocation lines with temperature is in correspondence with
4 the observed decrease of hardness after thermal ageing on a W material with higher rolling
5 degree in the work of Reiser *et al*. [52]).
6
7 **Table II**. Fitted parameters of eq.(6) to the experimental data for dislocation line and loop
8 densities (see text for details).

|	E (eV)	a_{irr} $m^{-3} \cdot day^{-1}$	τ_0 (day)
Loops	0.61	9.2×10^{22}	6×10^{-3}
Lines	0.095	$<10^{10}$	19.7

9

10 ### 3.1.2 *Open volume defects using PALS*

11 The normalized PALS spectra of the unirradiated and the irradiated W samples are
12 presented in Fig. 3. It is observed that after irradiation the average positron lifetime increases
13 compared to the unirradiated specimen.
14 As discussed in section 2.3.1 from PALS spectra the positron lifetimes in the defects present
15 in the material under investigation are determined. Therefore, the association of the
16 experimentally determined lifetimes with specific defects is essential. The lifetime that
17 corresponds to the defect-free W materials is reported to be in the range 100-116 ps [53, 54,
18 55, 56, 57, 58, 59]. The lifetimes for mono-vacancy and dislocation defects are reported in the
19 range of 160-200 ps and 130 – 180 ps, respectively [42, 55, 56, 60, 61]. The low lifetime value of
20 130 ps corresponds to screw dislocation as calculated by Staikov et al. [58]. Also the positron
21 lifetime of a vacancy associated to either screw or edge dislocation was calculated in the range
22 188-192 ps [58]. Therefore in the range of lifetimes 160-200 ps the defects to be associated
23 could be mono-vacancies and dislocations. The vacancy complex of 2-3 vacancies has been
24 found to exhibit a lifetime of 230 ps [62, 63]. Lifetime values from 200 to 380 ps have been
25 reported as equivalent to average cluster sizes containing 1 to 9 vacancies [62, 64]. Voids
26 having 13-37 vacancies have a lifetime of 410 - 440 ps [57], and a longest lifetime of 550 ps has
27 been associated with large vacancy clusters containing more than 40 vacancies [62]. Therefore
28 lifetimes above 200 ps are associated with vacancy agglomerates.
29 For the unirradiated sample two lifetimes are required to fit its PALS spectrum, a lifetime
30 τ_0 ~100 ps which according to the discussion above corresponds to positron annihilations in
31 the bulk defect free material and a second lifetime τ_1 having a value of (170 ± 1) ps which is

1 attributed to positron annihilations at dislocations (Fig. 4). These dislocations have been

2 created during the cold rolling fabrication process of the W material. The intensities I_0 and I_1

3 are almost equal demonstrating that the probabilities of a positron to be annihilated in the

4 defect free material or in the dislocations are equal. The high value of I_1 actually reflects the

5 high density of dislocations in the as fabricated material as it is presented in Table I containing

6 the TEM results.
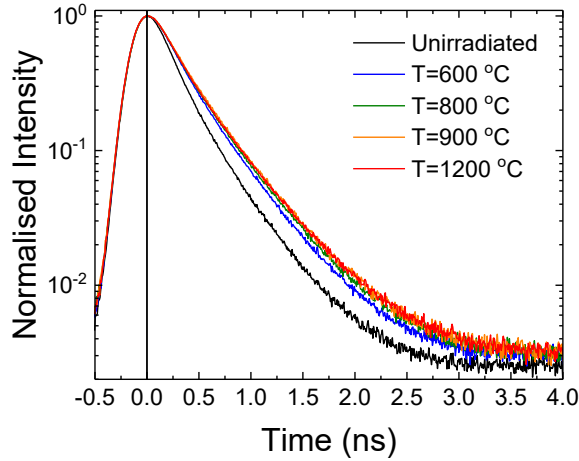
7

8 **Fig. 3.** PALS spectra for cold rolled W plate irradiated at 600, 800, 900 and 1200 ^{o}C and the

9 unirradiated one.

10

11

12 Three positron lifetime components (τ_0, τ_1 and τ_2) were required to describe the PALS

13 spectra for all the irradiated samples (Fig. 4). The obtained lifetimes with their average τ_{av}

14 together with their relative intensities versus irradiation temperature are presented in Fig. 3. In

15 the fitting procedure the lifetime τ_0 was kept constant to that found in the unirradiated sample.

16 The average lifetime shows a two-fold increase after irradiation at 600 °C, reflecting the

17 creation of extensive open volume defects, whereas it increases almost linearly with the

18 increase of the irradiation temperature from 600 to 900 °C. Further increase of the irradiation

19 temperature does not change its value significantly.

20 The lifetime, τ_1, after irradiation at 600 °C is (163 ± 1) ps, close to that found for the

21 unirradiated sample ((170 ± 1) ps). The defects associated with this lifetime in both the

22 unirradiated and irradiated samples are dislocations [42, 55, 56, 60, 61]. As the irradiation

23 temperature increases to 800 °C τ_1 increases to (205 ± 2) ps. This lifetime must be a weighted

24 average of lifetimes corresponding to very small vacancy clusters of about up to 3 vacancies.

25 Further increase of the irradiation temperature to 900 °C causes the increase of τ_1 to (246 ± 6)

26 ps which corresponds to a vacancy complex of 4-5 vacancies [57]. Irradiation at 1200 °C results

12

1 in the decrease of τ_1 to (156 ± 5) ps, similar to the values of the unirradiated sample and that

2 irradiated at 600 °C and reflecting positron annihilations at dislocations. Summarizing the

3 results for τ_1, for irradiation at 600 and 1200 °C τ_1 is associated with dislocations and with

4 probably vacancy-impurity complexes (as it will be discussed below) whereas at 800 and 900 °C

5 τ_1 is attributed to both dislocations and small vacancy clusters.

6   After irradiation a second lifetime, τ_2, is observed with values ranging from 492 to 553 ps.

7 This lifetime corresponds to positron annihilations at large vacancy clusters or voids having

8 more than 40 vacancies [57, 62]. The obtained values for τ_2 show that for irradiation at 600 °C

9 the voids have a diameter larger than about 1 nm, a value which is in agreement with TEM

10 results. The lifetime τ_2 increases almost linearly with the irradiation temperature up to 900 °C

11 and then it remains constant. The increase of τ_2 with irradiation temperature indicates larger

12 number of vacancies in a cluster. For large vacancy clusters (>40 vacancies) theoretical

13 calculations predict a small or no dependence of the positron lifetime on the void size [38, 57],

14 due to the localization of positron at the cavity surface, with a saturation positron lifetime value

15 of around 500 ps. Therefore, the increase of lifetime τ_2 with irradiation temperature reflects an

16 increase in the size of the vacancy clusters which is observed also by TEM.
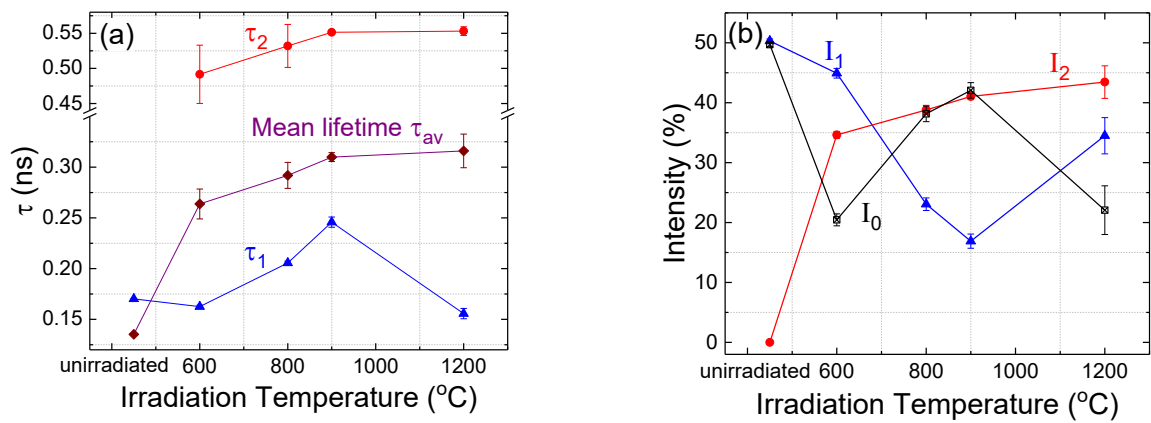
17

Fig. 4. Lifetime components (a) and their relative intensities (b) obtained from least square fit of equation (1) to PALS spectra for the unirradiated and irradiated cold rolled W plate at the various irradiation temperatures.

18   The intensities $I_i, (i=0,1,2)$, reflect the probability of a positron being annihilated within

19 the defect free matrix ($i=0$) or a defect ($i=1$ dislocation or monovacancy or small vacancy

20 complex of up to 5 vacancies, $i=2$ vacancy cluster of more than 40 vacancies). The relative

21 probabilities (I_i/I_0, $i=1,2$) reflect the extent of the defects in relation with the defect free

1 regions. In the unirradiated sample $I_1/I_0 \approx 1$, i.e. it is equal probable the positron to be

2 annihilated in a dislocation and in the defect free matrix. This indicates that ~50% of the sample

3 can be considered as affected by the dislocations introduced by the cold rolling.

4   Irradiation at 600 °C increases this ratio to around 2.2, reflecting the dislocations arising

5 from the irradiation. According to TEM results the total dislocation density increases from

6 1×10^{14} m^{-2} for the unirradiated sample to around 2.2×10^{14} m^{-2} for the sample irradiated at 600

7 °C (Table I, dislocation total density), and this increase is in excellent agreement with the

8 obtained ratio I_1/I_0. At 800 °C I_1/I_0 is reduced by a factor of about 4 and the same reduction

9 is observed in the dislocation density observed by TEM. As it has been discussed above there is

10 an increase in the lifetime τ_1 and this increase has been associated with small vacancy clusters.

11 As the decrease of the ratio I_1/I_0 at 800 °C is equivalent to the decrease of the dislocation

12 density the contribution of the vacancy clusters in I_1 could be assumed small. For the

13 irradiation at 1200 °C the ratio I_1/I_0 is 50 % higher than that of the unirradiated sample. On

14 the contrary, the observed dislocation density by TEM is by a factor of three lower. As these

15 two findings are inconsistent we might assume that other defects formed at 1200 °C and having

16 annihilation times close to that of dislocations contribute. Yabuuchi at al. [61] calculated a

17 positron lifetime of ~170 ps for the V-C, V-N, and V-O complexes and a lifetime of 169 ps for a

18 monovacancy decorated with two hydrogen atoms (V-2H) and 164 ps for a monovacancy

19 decorated with three hydrogen atoms (V-3H). However, at the irradiation temperature of 1200

20 °C vacancy-hydrogen (V-nH) clusters are not expected to be present because the dissociation of

21 hydrogen from vacancy takes place at much lower temperatures according to thermal

22 desorption spectroscopy studies [65]. As the intensity I_0 reflects the region of the material free

23 of defects, it can be concluded that the defect free volume of the material at 1200 °C is 50%

24 lower than that at 900 °C. It is improbable that vacancy-impurity complexes have generated

25 such a numerous number of defect complexes at the higher irradiation temperature. However,

26 at 1200 °C the volume of voids has been increased by a factor of nine compared to that at 800

27 °C (Table I). These larger voids generate a stress field around them which might act as a trap of

28 the positrons. In any case, further results are needed for a comprehensive explanation of the

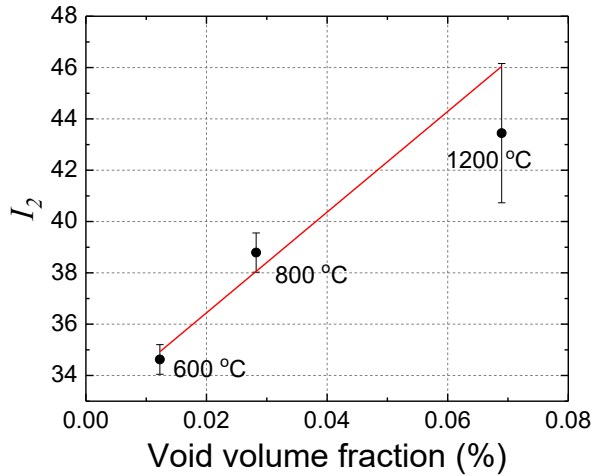29 considerable decrease of the defect free volume at 1200 °C.

30

Fig. 5. Intensity I_2 corresponding to voids obtained from least square fit of eq. (1) to PALS data versus void volume fraction as determined by TEM measurements (Table I). The solid line is a linear least square fit to the data.

As discussed above the lifetime τ_2 and consequently the intensity I_2 have been attributed to large vacancy clusters or voids. As the irradiation temperature increases the intensity I_2 and the lifetime τ_2 increase almost linearly (Fig. 4). This increase of I_2 indicates the respective increase in the volume fraction of vacancy clusters under the assumption that the trapping strength for positrons remains constant and it is in very good agreement with the void's volume fraction as determined from TEM results (Table I) as it is shown by its almost linear correlation with the volume fraction measured by TEM (Fig. 5).

2.3.2 Open volume defects using PAS-DB

In Fig. 6 the CDB spectra obtained at different irradiation temperatures are presented. The spectra focussed around the low momenta are shown in Fig. 6a, while the ones around the high momenta are presented in Fig. 6b. For the low momenta, the spectra for the irradiated samples increase significantly compared to the reference, while for the high momenta no obvious difference can be observed within the scatter. Although a measurable increase is measured for low momenta, little variation with irradiation temperature is observed. To check this increase in more depth, the S-parameter is computed. Computation of the W-parameter is omitted due to the large scatter (low statistics).

15
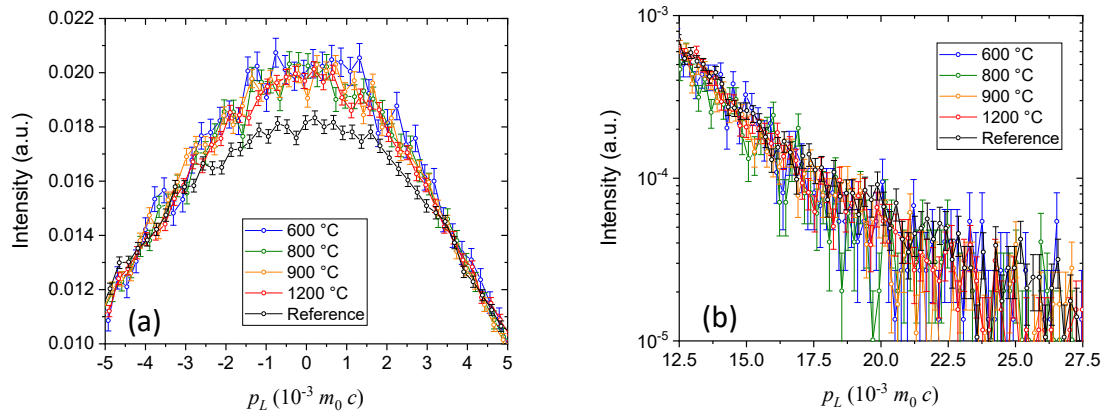
Fig. 6. CDB spectra for the different irradiation temperatures in the low momentum region (a), and high momentum region (b).

In Fig. 7 the *S*-parameter is presented as a function of irradiation temperature. Consistent with the CDB spectra, the *S*-parameter varies little with temperature: 11% at 600 °C and 8% at 1200 °C. Thus, even at the irradiation temperature of 1200 °C, a significant amount of open volume defects is still present in the material.

The slight decrease of *S*-parameter with irradiation temperature is consistent with a shift in vacancy cluster population towards larger clusters, as explained in [18]. This observation is consistent with the picture sketched following the PALS measurements.
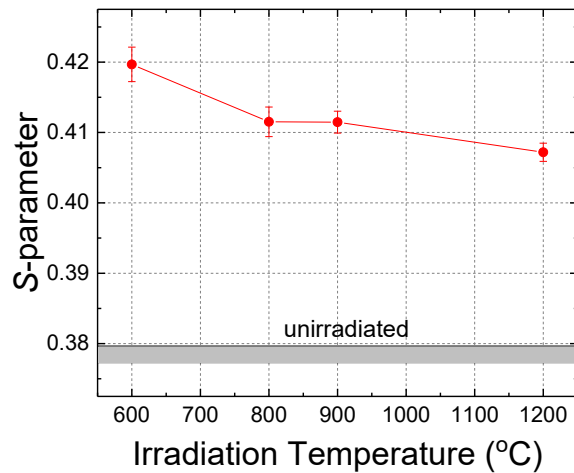

Fig. 7. *S*-parameter as a function of irradiation temperature.

1   ## 2.3.2 Electrical Resistivity

2   The electrical resistivity of the unirradiated W material was found to be
3    $(5.65 \pm 0.03)\ \mu\Omega\cdot cm$. In the literature the reported resistivity value of high purity (99.99% or
4   higher) W at 20 $^{\circ}$C is $5.28\ \mu\Omega\cdot cm$ for polycrystalline samples [66, 67]. The difference of
5    $0.37\ \mu\Omega\cdot cm$ between the resistivity of the W material used in the current study and the value
6   reported in the literature is due to the dislocations induced by the cold-rolling process as it will
7   be discussed below.

8   The resistivity of the irradiated samples was found higher than that of the unirradiated
9   reflecting the additional electron scattering from the irradiation induced defects and
10   transmutation products. By subtracting the resistivity of the unirradiated sample from that of
11   the samples irradiated at the various temperatures, the Radiation Induced Resistivity, RIR, is
12   derived. With this subtraction the electrical resistivity arising from the scattering of conduction
13   electrons from phonons and also scattering arising from dislocations or other defects produced
14   during the fabrication process of the material have been removed. Therefore, the result of this
15   subtraction refers to the resistivity increase caused by the irradiation, i.e. from additional
16   defects such as voids, dislocations and transmutation products.

17   The variation of RIR with the irradiation temperature is depicted in Fig. 8. The statistical
18   error from the voltage - current measurements are of the order of 10^{-3} $\mu\Omega$.cm or smaller. The
19   mean value and the experimental errors in Fig. 8, which are of the order of 10^{-2} $\mu\Omega$.cm, are
20   calculated from the variation of the resistivity for different in-plane orientations of the collinear
21   4-point probe. The RIR for irradiation at 600 $^{\circ}$C has the largest value compared to all the other
22   values measured for the irradiation temperatures 800 to 1200 $^{\circ}$C. The increase of the
23   irradiation temperature from 600 to 800 $^{\circ}$C causes a decrease of RIR of about 27%. At higher
24   irradiation temperatures RIR remains almost constant.

25   Further analysis of the electrical resistivity data requires their combination with available
26   data from TEM measurements through the use of a simple quantitative model for the scattering
27   of conduction electrons on the various types of defects and impurities. RIR can be considered
28   as the sum of four main components (ignoring cross scattering of the electrons from the
29   different defects)

30   $$RIR = RIR_{void} + RIR_{loop} + RIR_{line} + RIR_{trans} \tag{7}$$

31   where RIR_{void}, RIR_{loop}, RIR_{line} and RIR_{trans} are the contributions of voids (including mono- or
32   cluster of vacancies), dislocation loops, dislocation lines and transmutation products,
33   respectively.

34   The contribution of monovacancies to resistivity is proportional to their number density, if
35   their concentration is small (e.g. of the order of 10^{-3} or smaller) and they are randomly
36   distributed [68]. In the case of a vacancy cluster, a structure factor is needed for the description

1   of the relative position of vacancies inside it [69]. Detailed calculations for the determination of

2   the contribution of vacancy clusters to resistivity were performed by J. W. Martin et al. [70, 71,

3   72] and it was found that, for nearly spherical clusters, the corresponding resistivity can be

4   described approximately by a power law dependence on the number n_{vac} of the vacancies in a

5   cluster as

6   $$RIR_{\text{void}} \approx P_{1V} \cdot n_{vac}^{0.7} \cdot N_{\text{void}} = C \cdot (d_{void} / \alpha)^{2.1} \cdot N_{\text{void}} \tag{8}$$

7   where $P_{1V} \approx 10^{-34}$ $\Omega \cdot \text{m}^4$ [73] is the vacancy specific resistivity, i.e. the resistivity corresponding

8   to 1 monovacancy per m^3 and N_{void} (m^{-3}) is the number density of a vacancy cluster having n_{vac}

9   vacancies. For a void of diameter d_{void} the first term of eq. (8) results to the second one where

10   α the W lattice constant and C a known constant (1.033×10^{-26} $\mu\Omega \cdot \text{cm} \cdot \text{m}^3$). Using eq. (8) and

11   the density and diameter of the voids determined by TEM the RIR_{void} has been calculated and

12   it is presented in Table III. The voids have a small contribution to RIR of 1.4% at 600 °C which

13   increases to 4.6% at 1200 °C.

14   The transmutation products Re, Os and Ta have been evaluated by FISPACT-II nuclide

15   inventory code and TENDL-2017 and EAF-2010 nuclear data bases (to be published). The

16   calculated concentration for Os and Ta are about two orders of magnitude lower than that of

17   Re and therefore only Re is taken into account for the calculation of RIR arising from the

18   transmutation productions, thus

19   $$RIR_{trans} = P_{\text{Re}} N_{\text{Re}} \tag{9}$$

20   where $P_{\text{Re}} = 1.3$ $\mu\Omega \cdot \text{cm}/(\text{Re at.}\%)$ the specific resistivity applicable to dilute W-Re alloys [74,

21   75]. However, the calculated Re concentration depends on the nuclear data base used (TENDL-

22   17 or EAF-2010). The RIR_{trans} (eq. (9)) has been calculated for the two nuclear data bases and it

23   is shown in Fig. 8. The produced Re calculated using the two data bases differs of about 60%.

24   The different RIR_{trans} values for different irradiation temperatures are due to a slightly varying

25   neutron fluence at the irradiation positions. The RIR_{trans} values arising from EAF-2010 nuclear

26   data base and in the range 800 to 1200 °C are larger than the experimentally determined RIR

27   values corresponding to all the irradiation produced defects. This leads us to the conclusion

28   that the calculations based on EAF-2010 data base are inconsistent with the experimental data

29   and, thus, the calculations based to TENDL-2017 data base will be used further on.

30   Regarding the contribution of radiation induced dislocations to RIR, it is considered that

31   electrical resistivity due to dislocations is insensitive to the details of dislocation arrangement,

32   since the main contribution to dislocation resistivity emerges from scattering of conduction

33   electrons within a few Burgers lengths from dislocation lines [76] and, therefore, the effects of

34   the dislocation cores dominate those of the long-range strain fields [77]. Due to this

insensitivity to the details of dislocations arrangement, the contribution of dislocations to electrical resistivity is expressed as [78, 79, 80, 81]

$$RIR_{\text{line}} = P_{\text{DSR}} N_{\text{line}} \tag{10a}$$

where P_{DSR} the Dislocation Specific Resistivity, and N_{disl} the dislocation density. In the case of dislocation loops, eq. (10a) takes the form

$$RIR_{\text{loop}}(d_{\text{loop}}) = P_{\text{DSR}} \cdot \pi d_{\text{loop}} \cdot N_{\text{loop}}(d_{\text{loop}}) \tag{10b}$$

where d_{loop} is the diameter of the dislocation loop and $N_{\text{loop}}(d_{\text{loop}})$ their number density. Therefore the RIR from both lines and loops, RIR_{disl} , can be written as

$$R_{\text{disl}} = RIR_{\text{line}} + RIR_{\text{loop}} = P_{\text{DSR}} \left[N_{\text{line}} + \pi d_{\text{loop}} \cdot N_{\text{loop}}(d_{\text{loop}}) \right] \tag{11}$$

There is a discrepancy between the values reported in the literature for P_{DSR} of W where three different values are found for P_{DSR}: 7.5×10^{-25} $\Omega \cdot m^3$, 1.9×10^{-24} $\Omega \cdot m^3$ and 6.7×10^{-23} $\Omega \cdot m^3$ spanning two orders of magnitude [78, 79, 80, 81]. The measurement of P_{DSR} is based at measurements of deformed high purity materials at cryogenic temperatures (~4.2 K) where the contribution of electron-phonon scattering is practically zero, and the measured values are considered to be due to dislocations. However, impurities can never be completely removed and their presence may cause a correlation between electron-dislocation scattering and electron-impurity scattering in a metal, which results in the dependence of P_{DSR} on dislocation density [82, 83]. Dislocation densities smaller than a threshold value of about 10^{13} m^{-2} at 4.2 K can result in overestimation of P_{DSR} of an order of magnitude [81]. A.S. Karolik *et al*. [81] concluded that the value of 6.7×10^{-23} $\Omega \cdot m^3$ given for W in Ref. [79] is overestimated since it emerged from measurements in samples where the dislocation density was not high enough.

There is one limitation for comparing RIR experimental values versus the calculated ones. It arises from the fact that the Dislocation Specific Resistivity, P_{DSR} , is not well established (in the literature it varies by two orders of magnitude, see discussion above). As we require $RIR_{\text{exp}} = RIR_{calc}$ and taking into account eqs. (7)-(11) we have

$$RIR_{\text{exp}} = RIR_{calc} = RIR_{\text{trans,calc}} + RIR_{\text{void,calc}} + P_{\text{DSR}} \left(N_{\text{disl}} + \pi \cdot d_{\text{loop}} \cdot N_{\text{loop}} \right)$$
$$RIR_{\text{trans,calc}} \left(P_{\text{DSR}} \right) = \left(RIR_{\text{exp}} - RIR_{\text{void,calc}} \right) - P_{\text{DSR}} \left(N_{\text{disl}} + \pi \cdot d_{\text{loop}} \cdot N_{\text{loop}} \right) \tag{12}$$
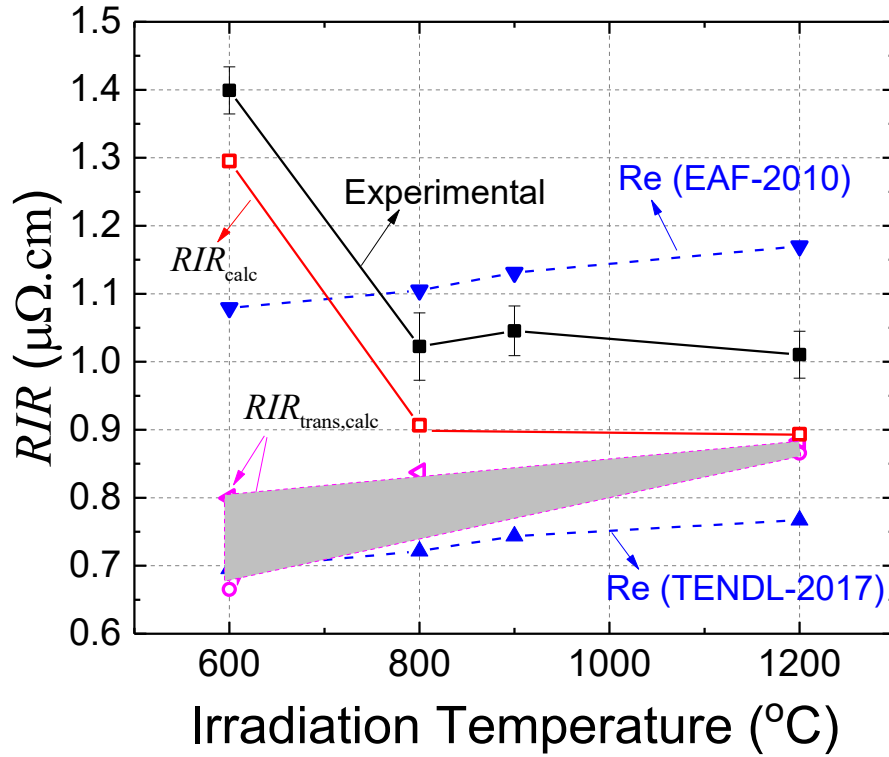
1
2 **Fig. 8**. Radiation induced resistivity, RIR, of the neutron irradiated cold rolled W plate samples
3 to 0.18 dpa at various irradiation temperatures. (■): experimental data, (□): calculated using
4 eq. (7) for $P_{\text{DSR}} = 2.6 \times 10^{-23}$ $\Omega \cdot \text{m}^3$ and Re production according to TENDL-2017, (▲, ▼):
5 RIR_{trans} calculated contribution from Re transmutation product using TENDL-2017 and EAF-
6 2010 nuclear data base, (○, ◁): $RIR_{\text{trans,calc}}$, the difference between experimental data and that
7 calculated values for the defects (voids, dislocations loops and lines) determined from the TEM
8 data in Table I and eqs. (8), (11) and (12), using for P_{DSR} the values of 2.6×10^{-23} $\Omega \cdot \text{m}^3$ (◁) and
9 3.2×10^{-23} $\Omega \cdot \text{m}^3$ (○) (see text for details).

10

11 As the densities of voids, dislocations and their sizes are known from TEM, $RIR_{\text{trans,calc}}\left(P_{\text{DSR}}\right)$ can
12 be calculated if the correct value of P_{DSR} is known. As this is not the case, we may use the fact
13 that $RIR_{\text{trans,calc}}\left(P_{\text{DSR}}\right)$ for the correct value of P_{DSR} should be a line almost parallel to x-axis as
14 the concentration of Re transmutation produced defects is almost constant versus
15 temperature. $RIR_{\text{trans,calc}}$ has been calculated for two values of P_{DSR} ($P_{\text{DSR}} = 2.6 \times 10^{-23}$ $\Omega \cdot \text{m}^3$ and
16 3.2×10^{-23} $\Omega \cdot \text{m}^3$) shown in Fig. 8. Values outside these limits give values with large slopes so
17 they have to be dismissed. Further we observe from Fig. 8 that $RIR_{\text{trans,calc}}$ is in satisfactory

agreement with that evaluated using the Re concentration obtained employing TENDL-2017 nuclear data base. Finally in Fig. 8 the calculated RIR, RIR_{calc}, using $P_{DSR} = 2.6 \times 10^{-23} \ \Omega \cdot m^3$ and RIR_{trans} evaluated using TENDL-2017 nuclear data base is compared with the experimental data and a reasonable agreement is obtained. The experimental and calculated values of resistivity as well the contribution of the different defects are presented in Table III in which a good agreement between calculated and experimental values is observed.

Table III. Experimental and calculated values for Radiation Induced Resistivity, RIR, for defects as determined from TEM measurements, and Re transmutation production using TENDL-2017 nuclear data base.

	Experimental	Calculated	Contribution to Calculated		
T_{irr}	RIR	RIR_{calc}	RIR_{trans}	RIR_{void}	RIR_{disl} [1]
(°C)	($\mu\Omega$.cm)	($\mu\Omega$.cm)	($\mu\Omega$.cm)	($\mu\Omega$.cm)	($\mu\Omega$.cm)
600	1.40 ± 0.05	1.30	0.70	0.019	0.58
800	1.02 ± 0.05	0.91	0.72	0.036	0.15
1200	1.01 ± 0.03	0.90	0.77	0.046	0.08

[1] For $P_{DSR} = 2.6 \times 10^{-23} \ \Omega \cdot m^3$

At the beginning of section 2.3.2 the difference of $0.37 \ \mu\Omega \cdot cm$ between the resistivity of the W material used in the current study and the value reported in the literature was attributed to the dislocations induced by the cold-rolling process. Using the obtained value of $2.6 \times 10^{-23} \ \Omega \cdot m^3$ for P_{DSR} the dislocation density was determined equal to 1.4×10^{14} m^{-2} for the unirradiated state of the W plate material. This value is in excellent agreement with that determined by TEM (Table I).

3.2   Mechanical Properties

3.2.1   Elastic Properties

The Young's modulus, E, shear modulus, G, and Poisson ratio, ν, of the non-irradiated and irradiated W plate were determined as described in Section 2.5 and are presented in Table IV. The values for the unirradiated sample are in a good agreement with literature data which are reported in the range 400 to 420 GPa, 158 to 163 GPa, and 0.278 to 0.282, for E, G and ν respectively [84, 85, 86]. As the irradiation temperature increases a systematic decrease is observed in the Young's and shear moduli and this decreases is of about 3.5% after irradiation at 1200 °C. This may related with the increase of the volume fraction of voids which presents a seven-fold increase as the irradiation temperature increases from 600 to 1200 °C.

The effects of radiation on metals are expected to be greatest in annealed materials and decreased in magnitude as lattice defects are introduced by cold work or heat-treatment. Taking into account that the reference material is heavily deformed it is expected that due to the fact that irradiation takes place at rather high temperatures there is an effect from the annealing itself, being of a duration of about 70 days, at the irradiation temperature. It is noted that irradiation and annealing, as already mentioned in 3.1.1, have a competing role in the microstructure and as a result in the mechanical properties of the material. The competing effect of annealing and radiation damage on the elastic properties is investigated in [87] on ITER grade W, which is less heavily deformed in the as fabricated condition compared to the material of the current work.

Table IV. Experimentally determined Young's modulus, E, shear modulus, G, Poisson's ratio, v, and Vickers hardness, H_V, of unirradiated and irradiated to 0.18 dpa cold rolled sheet W.

| T_{irr} (°C)	E (GPa)	G (GPa)	v	H_V (GPa)
Unirradiated	402 ± 3	158 ± 1	0.27 ± 0.03	4.77 ± 0.04
600	396 ± 6	155 ± 2	0.28 ± 0.03	5.61 ± 0.07
800	392 ± 6	154 ± 2	0.27 ± 0.03	5.97 ± 0.06
900	389 ± 6	153 ± 2	0.27 ± 0.03	5.84 ± 0.06
1200	388 ± 6	152± 2	0.28 ± 0.03	5.94 ± 0.08

3.2.2 Vickers hardness

From the optically determined diagonal of the Vickers' indenter imprint and eq. (4), the Vickers hardness of the material was determined (Table IV). The Vickers hardness, H_V, of the unirradiated cold rolled W plate material was found (4.77 ± 0.04) GPa. The Vickers hardness reported in [28] for the same reference W material (1 mm thickness) using a load of around 1 N is 5.8 GPa (592HV0.1). The lower value in the current work is probably related to the well-known indentation size effect (ISE) [88], wherein the hardness is observed to increase with decreasing indentation size, especially in the sub-micrometer depth regime, and it is attributed to the evolution of geometrically necessary dislocations beneath the indenter, which gives rise to the strain gradients that cause enhanced hardening. The indentation hardness measured for the same material at a load of 50 N with a Vickers' indenter in [29] has a value of (4.8 ± 0.1) GPa, which is very close to that of the current work. Although the indentation hardness is expected to be lower than the Vickers one by about 7% the similarity of the two hardness values can be accounted for taking into consideration ISE effects which result in lower hardness value as the load increases.

1 Irradiation to 0.18 dpa at 600 ^{o}C increases the hardness by 17 % while irradiation at higher
2 temperatures leads to a further increase of the hardness (Fig. 9). The highest hardness increase,
3 ΔH_{V}, of about 25% is observed after irradiation at 800 ^{o}C, while further increase of the
4 irradiation temperature does not affect hardness significantly.
5
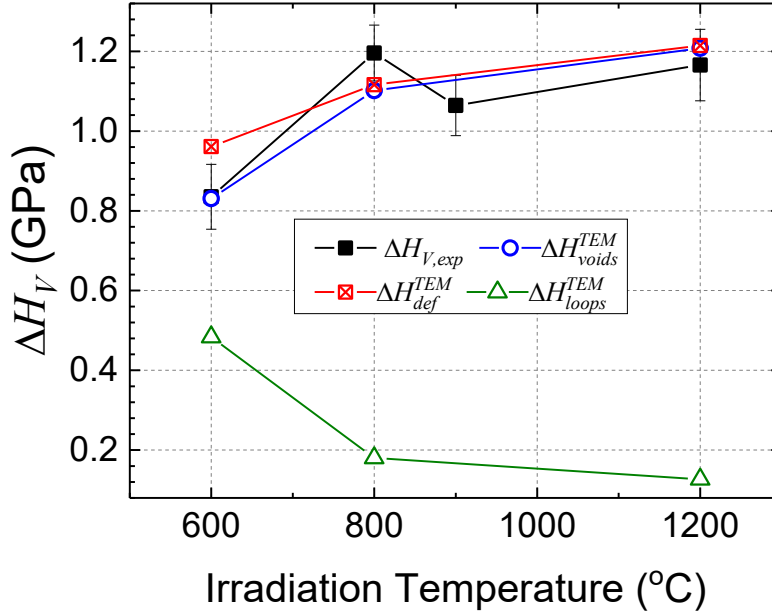
6
7 **Fig. 9.** Experimental (■) Vickers hardness increase versus irradiation temperature of cold rolled
8 W sheet irradiated to 0.18 dpa. Calculated contributions employing eqs. (15) and (16) and TEM
9 data (Table I) from voids (○), loops (△) and the total of defects (⊠) assuming root-sum-square
10 law.

11
12
13 Subsequently, the dispersion hardening barrier (DHB) model is used to describe the
14 radiation hardening in metals [11, 89]. According to the DHB model each type of defect induces
15 an increase in the yield strength, $\Delta\sigma_{def}$, that can be expressed as

16 $$\Delta\sigma_{def} = M\alpha_{def}Gb\sqrt{N_{def}d_{def}} \; , \qquad (13)$$

17 where M is the Taylor factor, α_{def} is the defect cluster barrier strength, G is the shear
18 modulus, b is the magnitude of the Burger's vector ($b = 0.274$ nm for W), N_{def} is the number
19 density of the defects, and d_{def} is the mean diameter of the defects. Combining eq. (13) with
20 the equation that correlates hardness and yield strength as proposed by Tabor [90]

21 $$H_{V} = k\sigma_{def} \; , \qquad (14)$$

23

1   the hardening, ΔH_V, induced by irradiation defects can be determined through

$$\Delta H_V = kM\alpha_{def}Gb\sqrt{N_{def}d_{def}}\,. \tag{15}$$

3   In Tabor's theory the proposed value of k is 2.74 [91]. However, Hu et al. [11], following the
4   work of Busby et al. [92], have proposed 3.20 as a more appropriate value of k. For the Taylor
5   factor, M, R.E. Stoller and S.J. Zinkle [93] have recommended the value of 3.06 for non-
6   textured BCC and FCC crystals. The same authors recommend the use of the value of 3.06 even
7   for textured crystals, as the W material of the current study, to provide a standard basis of
8   comparison when publishing results of microstructure-mechanical property correlations. The
9   value of the obstacle strength factor, α_{def}, depends on the type and size of the defects. For the
10   dislocation loops for α_{disl} the value of 0.15 was adopted as suggested in [11]. The obstacle
11   strength for voids depends on their size and taking into account the mean size of voids
12   measured by TEM we can develop a scaling using the measured values of hardness. Assuming a
13   root-sum-square law the measured hardening is connected with the voids and loop obstacles as

$$\Delta H_{calc}^2 = \Delta H_{loop}^2 + \Delta H_{void}^2 = \left(kMGb\right)^2\left(\alpha_{loop}^2 N_{loop}d_{loop} + \alpha_{void}^2\left(d_{void}\right)N_{void}d_{void}\right) \tag{16}$$

15   Setting $\Delta H_{calc} = \Delta H_{V,\exp}$ we can calculate $\alpha_{void}\left(d_{void}\right)$ since all the other values are known. The
16   α_{void} has been calculated in Fig. 10 using relevant TEM values and for k, M and α_{disl} the values
17   suggested by Hu et al [11], and for the shear modulus, G, that measured employing IET (Table
18   IV). We observe that α_{void} and the void size, d_{void}, are well correlated, and the obtained values
19   are in good agreement with those obtained by Hu for the corresponding sizes. Finally the
20   hardness arising from the loop and the voids as well the total hardness are calculated (Table IV).
21   As it can be observed in Fig. 9 and Table V the calculated hardening, ΔH_{def}^{TEM}, is in good
22   agreement with the experimental values within error. At 600 °C the contribution from loops to
23   the hardening is comparable with that from voids, whereas at 1200 °C the hardening is mainly
24   due to the voids and the loops have a minor contribution because of the drastic decrease in
25   their number density.
26   It is noted that the evolution of microstructure, and as a result that of hardness, versus
27   irradiation temperature is governed by the competing effects of damage recovery at the high
28   irradiation temperature and by damage formation. The separation of these two mechanisms is
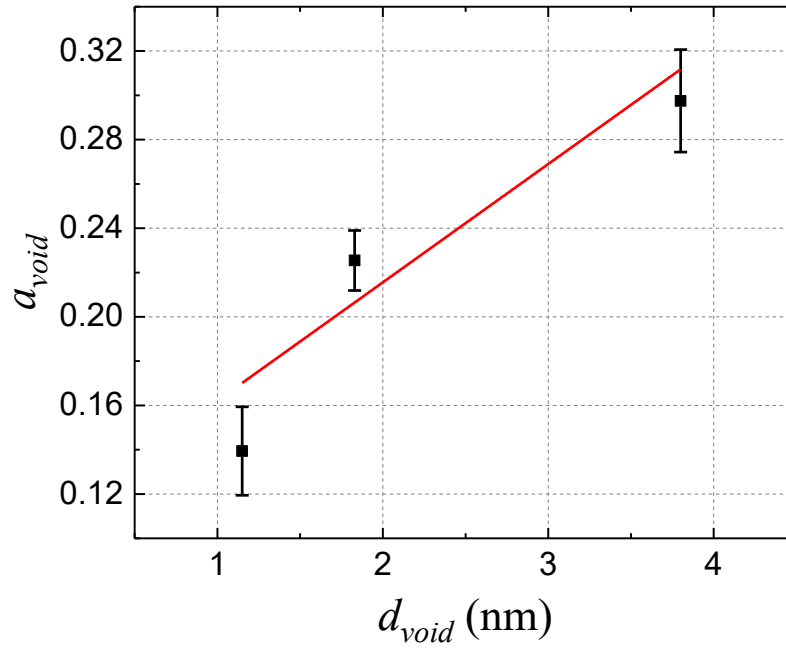29   outside the scope of the current work.
30
31

Fig. 10. Obstacle strength versus void diameter calculated using eq. (16). The solid line is a linear least square fit to the data.

Table V. Experimental Vickers hardness increase, ΔH_V, and calculated one using the dispersion barrier hardening model and the data obtained from TEM measurements (Table I).

T_{irr} (°C)	$\Delta H_{V,\exp}$ (GPa)	ΔH_{voids} (GPa)	α_{void}[1]	ΔH_{loops} (GPa)	ΔH_{calc}[2] (GPa)
600	0.84 ± 0.08	0.83	0.17	0.48	0.96
800	1.20 ± 0.07	1.10	0.21	0.18	1.12
1200	1.17 ± 0.09	1.21	0.31	0.13	1.21

[1]From the least squares fitted line in Fig.10.

[2]$\Delta H_{calc} = \sqrt{\Delta H_{loop}^2 + \Delta H_{void}^2}$

4 SUMMARY AND CONCLUSIONS

Disks of tungsten material produced by PLANSEE SE by sintering and rolling to 1 mm thickness were irradiated by fast neutrons to a damage level of 0.18 dpa and in the temperature range from 600 to 1200 °C.

Voids and dislocation loops are observed at all irradiation temperatures, with their number density decreasing and their size increasing with the increase of the irradiation temperature. This microstructural evolution should be perceived as the result of the rivalling factors of radiation damage production and recovery due to the annealing at the corresponding irradiation temperature. The total dislocation density after irradiation at 600 °C increases by a factor of two compared with that of the unirradiated sample. This increase is explained by a relatively high density of the dislocation loops formed. As the irradiation temperature is raised to 800 °C the total density of dislocation decreases showing that at this temperature pre-existing dislocations are removed during the irradiation. In general, the neutron irradiation reduces the density of pre-existing bulk dislocations by a factor of three. Voids are formed after irradiation at 600 °C having a mean size of around 1.15 nm. An increase of the irradiation temperature to 800 °C increases their size to 1.83 nm and their volume fraction by around three times. Further increase of the irradiation temperature to 1200 °C increases their volume fraction by a factor of two. These TEM observations are corroborated by positron annihilation spectroscopy results that show the formation of voids at all investigated irradiation temperatures with size larger than 1 nm. Furthermore, PALS also shows the formation of very small vacancy clusters in the temperature range of 800 - 900 °C.

The irradiation induced resistivity is in good agreement with the calculated values taking into account the partial contribution to the resistivity from transmutation, voids and dislocations. Therefore, three techniques TEM, positron annihilation spectroscopy and resistivity measurements give a consistent picture of the defects produced after 0.18 dpa fast neuron irradiation in the temperature range from 600 to 1200 °C.

A systematic decrease in the values of Young's and shear moduli is observed as the irradiation temperature increases and this decrease is of about 3.5% after irradiation at 1200 °C. This may be due to the increase of the volume fraction of voids which presents a seven-fold increase after irradiation at 1200 °C compared to that after irradiation at 600 °C. The Vickers hardness after irradiation at 600 °C has increased, compared to the unirradiated sample, by 0.83 GPa. Irradiation at 800 °C results to a further increase of 0.36 GPa. Higher temperature irradiation does not change the hardness, within errors, with respect to that measured at 800 °C. The hardness increase is mainly due to the voids and the higher the irradiation temperature the lower the effect from the dislocation loops is. The irradiation induced hardness is in good agreement with the values calculated using the dispersion hardening barrier model.

1 **References**

[1] M. Rieth, R. Doerner, A. Hasegawa, Y. Ueda, M. Wirtz, Behavior of tungsten under irradiation and plasma interaction, J. Nucl. Mater. 519 (2019) 334–368. https://doi.org/10.1016/j.jnucmat.2019.03.035.

[2] G. Pintsuk, Tungsten as a Plasma-Facing Material, in: Compr. Nucl. Mater., Elsevier, 2012: pp. 551–581. https://doi.org/10.1016/B978-0-08-056033-5.00118-X.

[3] S. Wurster, N. Baluc, M. Battabyal, T. Crosby, J. Du, C. García-Rosales, A. Hasegawa, A. Hoffmann, A. Kimura, H. Kurishita, R.J. Kurtz, H. Li, S. Noh, J. Reiser, J. Riesch, M. Rieth, W. Setyawan, M. Walter, J.H. You, R. Pippan, Recent progress in R&D on tungsten alloys for divertor structural and plasma facing materials, J. Nucl. Mater. 442 (2013) 181–189. https://doi.org/10.1016/j.jnucmat.2013.02.074.

[4] J. Reiser, J. Hoffmann, U. Jäntsch, M. Klimenkov, S. Bonk, C. Bonnekoh, M. Rieth, A. Hoffmann, T. Mrotzek, Ductilisation of tungsten (W): On the shift of the brittle-to-ductile transition (BDT) to lower temperatures through cold rolling, Int. J. Refract. Met. Hard Mater. 54 (2016) 351–369. https://doi.org/10.1016/j.ijrmhm.2015.09.001.

[5] C. Bonnekoh, A. Hoffmann, J. Reiser, The brittle-to-ductile transition in cold rolled tungsten: On the decrease of the brittle-to-ductile transition by 600 K to − 65 °C, Int. J. Refract. Met. Hard Mater. 71 (2018) 181–189. https://doi.org/10.1016/j.ijrmhm.2017.11.017.

[6] A. Hasegawa, T. Tanno, S. Nogami, M. Satou, Property change mechanism in tungsten under neutron irradiation in various reactors, J. Nucl. Mater. 417 (2011) 491–494. https://doi.org/10.1016/j.jnucmat.2010.12.114.

[7] A. Hasegawa, M. Fukuda, T. Tanno, S. Nogami, Neutron irradiation behavior of tungsten, Mater. Trans. 54 (2013) 466–471. https://doi.org/10.2320/matertrans.MG201208.

[8] A. Hasegawa, M. Fukuda, S. Nogami, K. Yabuuchi, Neutron irradiation effects on tungsten materials, Fusion Eng. Des. 89 (2014) 1568–1572. https://doi.org/10.1016/j.fusengdes.2014.04.035.

[9] A. Hasegawa, M. Fukuda, K. Yabuuchi, S. Nogami, Neutron irradiation effects on the microstructural development of tungsten and tungsten alloys, J. Nucl. Mater. 471 (2016) 175–183. https://doi.org/10.1016/j.jnucmat.2015.10.047.

[10] X. Hu, T. Koyanagi, M. Fukuda, Y. Katoh, L.L. Snead, B.D. Wirth, Defect evolution in single crystalline tungsten following low temperature and low dose neutron irradiation, J. Nucl. Mater. 470 (2016) 278–289. https://doi.org/10.1016/j.jnucmat.2015.12.040.

[11] X. Hu, T. Koyanagi, M. Fukuda, N.A.P.K. Kumar, L.L. Snead, B.D. Wirth, Y. Katoh, Irradiation hardening of pure tungsten exposed to neutron irradiation, J. Nucl. Mater. 480 (2016) 235–243. https://doi.org/10.1016/j.jnucmat.2016.08.024.

[12] M. Fukuda, N.A.P. Kiran Kumar, T. Koyanagi, L.M. Garrison, L.L. Snead, Y. Katoh, A. Hasegawa, Neutron energy spectrum influence on irradiation hardening and microstructural development of tungsten, J. Nucl. Mater. 479 (2016) 249–254. https://doi.org/10.1016/j.jnucmat.2016.06.051.

[13] T. Koyanagi, N.A.P.K. Kumar, T. Hwang, L.M. Garrison, X. Hu, L.L. Snead, Y. Katoh, Microstructural evolution of pure tungsten neutron irradiated with a mixed energy spectrum, J. Nucl. Mater. 490 (2017) 66–74. https://doi.org/10.1016/j.jnucmat.2017.04.010.

[14] L. M. Garrison, Y. Katoh, J. W. Geringer, M. Akiyoshi, X. Chen, M. Fukuda, A. Hasegawa, T. Hinoki, X. Hu, T. Koyanagi, E. Lang, M. McAlister, J. McDuffee, T.Miyazawa, C. Parish, E. Proehl, N. Reid, J. Robertson, & H. Wang, PHENIX U.S.-Japan Collaboration Investigation of Thermal and Mechanical Properties of Thermal Neutron–Shielded Irradiated Tungsten, Fusion Science and Technology 75(6) (2019) 499–509. https://doi.org/10.1080/15361055.2019.1602390

[15] T. Miyazawa, L. M. Garrison, J. W. Geringer, M. Fukuda, Y. Katoh, T. Hinoki, & A. Hasegawa, Neutron irradiation effects on the mechanical properties of powder metallurgical processed tungsten alloys, J. Nucl. Mater. 529 (2019) 151910. https://doi.org/10.1016/j.jnucmat.2019.151910

[16] T. Miyazawa, L. M. Garrison, J. W. Geringer, J. R. Echols, M. Fukuda, Y. Katoh, T. Hinoki, & A. Hasegawa, Tensile properties of powder-metallurgical-processed tungsten alloys after neutron irradiation near recrystallization temperatures, J. Nucl. Mater. 542 (2020) 152505. https://doi.org/10.1016/j.jnucmat.2020.152505

[17] L.M. Garrison, Y. Katoh, N.A.P.K. Kumar, Mechanical properties of single-crystal tungsten irradiated in a mixed spectrum fission reactor, J. Nucl. Mater. 518 (2019) 208–225. https://doi.org/10.1016/j.jnucmat.2019.02.050.

[18] G. Bonny, M.J. Konstantinovic, A. Bakaeva, C. Yin, N. Castin, K. Mergia, V. Chatzikos, S. Dellis, T. Khvan, A. Bakaev, A. Dubinko, D. Terentyev, Trends in vacancy distribution and hardness of high temperature neutron irradiated single crystal tungsten, Acta Mater. 198 (2020) 1–9. https://doi.org/10.1016/j.actamat.2020.07.047.

[19] R.K. Williams, F.W. Wiffen, J. Bentley, J.O. Stiegler, Irradiation induced precipitation in tungsten based, W-Re alloys, Metall. Trans. A. 14 (1983) 655–666. https://doi.org/10.1007/BF02643781.

[20] Y. Nemoto, A. Hasegawa, M. Satou, K. Abe, Microstructural development of neutron irradiated W-Re alloys, J. Nucl. Mater. 283–287 (2000) 1144–1147. https://doi.org/10.1016/S0022-3115(00)00290-7.

[21] M. Fukuda, A. Hasegawa, T. Tanno, S. Nogami, H. Kurishita, Property change of advanced tungsten alloys due to neutron irradiation, J. Nucl. Mater. 442 (2013) S273–S276. https://doi.org/10.1016/j.jnucmat.2013.03.058.

[22] M. Fukuda, K. Yabuuchi, S. Nogami, A. Hasegawa, T. Tanaka, Microstructural development of tungsten and tungsten-rhenium alloys due to neutron irradiation in HFIR, J. Nucl. Mater. 455 (2014) 460–463. https://doi.org/10.1016/j.jnucmat.2014.08.002.

[23] J. C. He, G. Y. Tang, A. Hasegawa, K. Abe, Microstructural development and irradiation hardening of W and W–(3–26) wt%Re alloys after high-temperature neutron irradiation to 0.15 dpa, Nucl. Fusion. 46 (2006) 877–883. https://doi.org/10.1088/0029-5515/46/11/001.

[24] S. Das, Recent advances in characterising irradiation damage in tungsten for fusion power, SN Appl. Sci. 1 (2019) 1–20. https://doi.org/10.1007/s42452-019-1591-0.

[25] M. Dürrschnabel, M. Klimenkov, U. Jäntsch, M. Rieth, H.C. Schneider, & D. Terentyev, New insights into microstructure of neutron - irradiated tungsten, Nature Scientific Reports (2021) 1–17. https://doi.org/10.1038/s41598-021-86746-6

[26] S. Dellis, X. Xiao, D. Terentyev, K. Mergia, S. Krimpalis, A. Bakaev, S. Messoloras, Mechanical properties of neutron-irradiated single crystal tungsten W(100) studied by indentation and FEM modelling, J. Nucl. Mater. (2021) 152985. https://doi.org/10.1016/j.jnucmat.2021.152985

[27] V.K. Sikka, J. Moteff, Superlattice of voids in neutron-irradiated tungsten, J. Appl. Phys. 43 (1972) 4942–4944. https://doi.org/10.1063/1.1661050.

[28]   S. Bonk, J. Reiser, J. Hoffmann, & A. Hoffmann, Cold rolled tungsten (W) plates and foils: Evolution of the microstructure. International Journal of Refractory Metals and Hard Materials 60 (2016) 92–98. https://doi.org/10.1016/j.ijrmhm.2016.06.020

[29] S. Krimpalis, K. Mergia, S. Messoloras, A. Dubinko, D. Terentyev, K. Triantou, J. Reiser, G. Pintsuk, Comparative study of the mechanical properties of different tungsten materials for fusion applications, Phys. Scr. 2017 (2017). https://doi.org/10.1088/1402-4896/aa9292.

[30] D. Pelowitz, J. Durkee, J. Elson, M. Fensin, R. Johns, G. McKinney, S. Mashnik, J. Verbeke, L. Waters, T. Wilcox, MCNPX 2.7.0 Extensions, 2011

[31] M.J. Norgett, M.T. Robinson, I.M. Torrens, A proposed method of calculating displacement dose rates, Nucl. Eng. Des. 33 (1975) 50–54. https://doi.org/10.1016/0029-5493(75)90035-7.

[32] P. Hirsch, A. Howie, R. Nicholson, D.W. Pashley, M.J. Whelan, Electron Microscopy of Thin Crystals, Krieger Publishing Company Malabar, Florida, 1977

[33] A. Dubinko, D. Terentyev, A. Bakaeva, K. Verbeken, M. Wirtz, M. Hernández-Mayoral, Evolution of plastic deformation in heavily deformed and recrystallized tungsten of ITER specification studied by TEM, Int. J. Refract. Met. Hard Mater. 66 (2017) 105–115. https://doi.org/10.1016/j.ijrmhm.2017.03.004.

[34] A. Dubinko, D. Terentyev, A. Bakaeva, T. Pardoen, M. Zibrov, T.W. Morgan, Effect of high flux plasma exposure on the micro-structural and -mechanical properties of ITER specification tungsten, Nucl. Instruments Methods Phys. Res. Sect. B Beam Interact. with Mater. Atoms. 393 (2017) 155–159. https://doi.org/10.1016/j.nimb.2016.10.041.

[35] A. Dubinko, D. Terentyev, A. Bakaeva, M. Hernández-Mayoral, G. De Temmerman, L. Buzi, J.M. Noterdaeme, B. Unterberg, Sub-surface microstructure of single and polycrystalline tungsten after high flux plasma exposure studied by TEM, Appl. Surf. Sci. 393 (2017) 330–339. https://doi.org/10.1016/j.apsusc.2016.09.071.

[36] A. Dubinko, A. Bakaeva, M. Hernández-Mayoral, D. Terentyev, G. De Temmerman, J.M. Noterdaeme, Microstructural modifications in tungsten induced by high flux plasma exposure: TEM examination, Phys. Scr. 2016 (2016). https://doi.org/10.1088/0031-8949/T167/1/014030.

[37] Positrons in Solids, in: P. Hautojarvi (Ed.), Topics in Current Physics, Vol. 12, Springer-Verlag Berlin Heidelberg, New York, 1979. https://doi.org/10.1007/978-3-642-81316-0.

[38] M. Eldrup, B.N. Singh, Studies of defects and defect agglomerates by positron annihilation spectroscopy, J. Nucl. Mater. 251 (1997) 132–138. https://doi.org/10.1016/S0022-3115(97)00221-3.

[39] D. Giebel, J. Kansy, LT10 Program for Solving Basic Problems Connected with Defect Detection, Phys. Procedia. 35 (2012) 122–127. https://doi.org/10.1016/j.phpro.2012.06.022.

[40] D. Giebel, J. Kansy, A new version of LT program for Positron Lifetime Spectra Analysis, Mater. Sci. Forum. 666 (2011) 138–141. https://doi.org/10.4028/www.scientific.net/MSF.666.138.

[41] G. Dlubek, A. Sen Gupta, J. Pionteck, R. Häßler, R. Krause-Rehberg, H. Kaspar, K.H. Lochhaas, Glass transition and free volume in the mobile (MAF) and rigid (RAF) amorphous fractions of semicrystalline PTFE: a positron lifetime and PVT study, Polymer (Guildf). 46 (2005) 6075–6089. https://doi.org/10.1016/j.polymer.2005.04.090.

[42] O. V. Ogorodnikova, M. Majerle, V. V. Gann, J. Čížek, P. Hruška, S. Simakov, M. Štefánik, V. Zach, Verification of the theory of primary radiation damage by comparison with experimental data, J. Nucl. Mater. 525 (2019) 22–31. https://doi.org/10.1016/j.jnucmat.2019.07.019.

[43] G.S. Kanda, L. Ravelli, B. Löwe, W. Egger, D.J. Keeble, Positron annihilation lifetime spectroscopy study of Kapton thin foils, J. Phys. D. Appl. Phys. 49 (2016) 025305. https://doi.org/10.1088/0022-3727/49/2/025305.

[44] M.J. Konstantinović, G. Bonny, Thermal stability and the structure of vacancy-solute clusters in iron alloys, Acta Mater. 85 (2015) 107–111. https://doi.org/10.1016/j.actamat.2014.11.026.

[45] M.J. Konstantinović, I. Uytdenhouwen, G. Bonny, N. Castin, L. Malerba, P. Efsing, Radiation induced solute clustering in high-Ni reactor pressure vessel steel, Acta Mater. 179 (2019) 183–189. https://doi.org/10.1016/j.actamat.2019.08.028.

[46] R.A. Weller, An algorithm for computing linear four-point probe thickness correction factors, Rev. Sci. Instrum. 72 (2001) 3580–3586. https://doi.org/10.1063/1.1394186.

[47] I. Miccoli, F. Edler, H. Pfnür, C. Tegenkamp, The 100th anniversary of the four-point probe technique: The role of probe geometries in isotropic and anisotropic systems, J. Phys. Condens. Matter. 27 (2015). https://doi.org/10.1088/0953-8984/27/22/223201.

[48] G. Martinček, The determination of poisson's ratio and the dynamic modulus of elasticity from the frequencies of natural vibration in thick circular plates, J. Sound Vib. 2 (1965) 116–127. https://doi.org/10.1016/0022-460X(65)90089-1.

[49] ASTM Standard E1876–01, Standard Test Method for Dynamic Young's Modulus, Shear Modulus, and Poisson's Ratio by Impulse Excitation of Vibration, ASTM Int. (2005) 16. doi:10.1520/E1876-09.

[50] A. Dubinko , D. Terentyev, C.Yin, W. Van Renterghem, B. Rossaert, M. Rieth, E. E. Zhurkin, A. Zinovev, C.-C. Chang, S. Van Dyck, & G. Bonny, Microstructure and hardening induced by neutron irradiation in single crystal, ITER specification and cold rolled tungsten. International Journal of Refractory Metals and Hard Materials 98 (2021) 105522. https://doi.org/10.1016/j.ijrmhm.2021.105522.

[51] L. Karanja, M. Lenci, D. Piot, C. Maurice, A. Durif, M. Richou, L. Gallais, M. Minissale & G. Kermouche, An Attempt to Assess Recovery / Recrystallization Kinetics in Tungsten at High Temperature Using Statistical Nanoindentation Analysis, Crystals 11 (2021) 37 https://doi.org/10.3390/cryst11010037

[52] J. Reiser, C. Bonnekoh, T. Karcher, W. Pfleging, D. Weygand, & A. Hoffmann, Recrystallisation towards a single texture component in heavily cold rolled tungsten (W) sheets and its impact on micromechanics. International Journal of Refractory Metals and Hard Materials 86 (2020) 105084. https://doi.org/10.1016/j.ijrmhm.2019.105084

[53] J.M. Campillo Robles, F. Plazaola, Collection of data on positron lifetimes and vacancy formation energies of the elements of the periodic table, Defect Diffus. Forum. 213–215 (2003) 141–236. https://doi.org/10.4028/www.scientific.net/ddf.213-215.141.

[54] M.J. Puska, Ab-initio calculation of positron annihilation rates in solids, J. Phys. Condens. Matter. 3 (1991) 3455–3469. https://doi.org/10.1088/0953-8984/3/20/007.

[55] T.E.M. Staab, R. Krause-Rehberg, B. Vetter, B. Kieback, The influence of microstructure on the sintering process in crystalline metal powders investigated by positron lifetime spectroscopy: I. Electrolytic and spherical copper powders, J. Phys. Condens. Matter. 11 (1999) 1757–1786. https://doi.org/10.1088/0953-8984/11/7/009.

[56] S. Zhu, Y. Xu, Z. Wang, Y. Zheng, D. Zhou, E. Du, D. Yuan, M. Fukuda, M. Mihara, K. Matsuta, T. Minamisono, Positron annihilation lifetime spectroscopy on heavy ion irradiated stainless steels and tungsten, J. Nucl. Mater. 343 (2005) 330–332. https://doi.org/10.1016/j.jnucmat.2004.11.024.

[57] T. Troev, E. Popov, N. Nankov, T. Yoshiie, Model calculation of positron states in tungsten containing hydrogen and helium, J. Phys. Conf. Ser. 207 (2010). https://doi.org/10.1088/1742-6596/207/1/012033.

[58] P. Staikov, N. Djourelov, Simulations of ⟨1 0 0⟩ edge and 1/2 ⟨1 1 1⟩ screw dislocations in α-iron and tungsten and positron lifetime calculations, Phys. B Condens. Matter. 413 (2013) 59–63. https://doi.org/10.1016/j.physb.2012.12.026.

[59] J. Heikinheimo, K. Mizohata, J. Räisänen, T. Ahlgren, P. Jalkanen, A. Lahtinen, N. Catarino, E. Alves, F. Tuomisto, Direct observation of mono-vacancy and self-interstitial recovery in tungsten, APL Mater. 7 (2019). https://doi.org/10.1063/1.5082150.

[60] P.E. Lhuillier, M.F. Barthe, P. Desgardin, W. Egger, P. Sperr, Positron annihilation studies on the nature and thermal behaviour of irradiation induced defects in tungsten, Phys. Status Solidi. 6 (2009) 2329–2332. https://doi.org/10.1002/pssc.200982114.

[61] A. Yabuuchi, M. Tanaka, A. Kinomura, Short positron lifetime at vacancies observed in electron-irradiated tungsten: Experiments and first-principles calculations, J. Nucl. Mater. 542 (2020) 152473. https://doi.org/10.1016/j.jnucmat.2020.152473.

[62] X. Hu, T. Koyanagi, M. Fukuda, Y. Katoh, L.L. Snead, B.D. Wirth, Defect evolution in single crystalline tungsten following low temperature and low dose neutron irradiation, J. Nucl. Mater. 470 (2016) 278–289. https://doi.org/10.1016/j.jnucmat.2015.12.040.

[63] C.L. Dube, P.K. Kulriya, D. Dutta, P.K. Pujari, Y. Patil, M. Mehta, P. Patel, S.S. Khirwadkar, Positron annihilation lifetime measurement and X-ray analysis on 120 MeV Au+7 irradiated polycrystalline tungsten, J. Nucl. Mater. 467 (2015) 406–412. https://doi.org/10.1016/j.jnucmat.2015.05.029.

[64] P.M.G. Nambissan, P. Sen, Positron annihilation study of the annealing behaviour of alpha induced defects in tungsten, Radiat. Eff. Defects Solids. 124 (1992) 215–221. https://doi.org/10.1080/10420159208220193.

[65] O. V. Ogorodnikova, B. Tyburska, V. K. Alimov, & K. Ertl, The influence of radiation damage on the plasma-induced deuterium retention in self-implanted tungsten, J. Nucl. Mater. 415 (2011) S661–S666. https://doi.org/10.1016/j.jnucmat.2010.12.012

[66] P.D. Desai, T.K. Chu, H.M. James, C.Y. Ho, Electrical Resistivity of Selected Elements, J. Phys. Chem. Ref. Data. 13 (1984) 1069–1096. https://doi.org/10.1063/1.555723.

[67] G.K. White, M.L. Minges, Thermophysical properties of some key solids: An update, Int. J. Thermophys. 18 (1997) 1269–1327. https://doi.org/10.1007/BF02575261.

[68] P.L. Rossiter, The electrical resistivity of metals and alloys, Cambridge University Press, Cambridge, 1987, pp. 195-198. https://doi.org/10.1017/CBO9780511600289.

[69] P.L. Rossiter, The electrical resistivity of metals and alloys, Cambridge University Press, Cambridge, 1987, pp. 127-136, pp. 195-198. https://doi.org/10.1017/CBO9780511600289.

[70] J.W. Martin, The electrical resistivity due to structural defects, Philos. Mag. 24 (1971) 555–566. https://doi.org/10.1080/14786437108217029.

[71] J.W. Martin, The electrical resistivity of some lattice defects in FCC metals observed in radiation damage experiments, J. Phys. F Met. Phys. 2 (1972) 842–853. https://doi.org/10.1088/0305-4608/2/5/008.

[72] J.W. Martin, R. Paetsch, Electrical resistivity of voids, J. Phys. F Met. Phys. 3 (1973) 907–917. https://doi.org/10.1088/0305-4608/3/5/005.

[73] K.D. Rasch, R.W. Siegel, H. Schultz, Quenching and recovery investigations of vacancies in tungsten, Philos. Mag. A Phys. Condens. Matter, Struct. Defects Mech. Prop. 41 (1980) 91–117. https://doi.org/10.1080/01418618008241833.

[74] L. Uray, P. Tekula-Buxbaum, Resistivity contribution of solutes in tungsten, J. Less-Common Met. 123 (1986) 95–100. https://doi.org/10.1016/0022-5088(86)90119-0.

[75] ASM Handbook Volume 2: Properties and Selection – Nonferrous Alloys and Special-Purpose Materials", ASM International, (1992), p. 1766.

[76] B.R. Watts, The contribution of the long-range strain field of dislocations in metals to their electrical resistivity, J. Phys. F Met. Phys. 18 (1988) 1183–1195. https://doi.org/10.1088/0305-4608/18/6/021.

[77] R.A. Brown, Resonance Scattering and the Electrical and Thermal Resistivities Associated with Extended Defects in Crystals, Phys. Rev. 156 (1967) 692–700. https://doi.org/10.1103/PhysRev.156.692.

[78] Z.S. Basinski, J.S. Dugdale, A. Howie, The electrical resistivity of dislocations, Philos. Mag. 8 (1963) 1989–1997. https://doi.org/10.1080/14786436308209092.

[79] H.B. Shukovsky, R.M. Rose, J. Wulff, The low temperature electrical resistivity of lattice defects in deformed tungsten single crystals, Acta Metall. 14 (1966) 821–830. https://doi.org/10.1016/0001-6160(66)90002-2.

[80] R.A. Brown, Electrical resistivity of dislocations in metals, J. Phys. F Met. Phys. 7 (1977) 1283–1295. https://doi.org/10.1088/0305-4608/7/7/026.

[81] A.S. Karolik, A.A. Luhvich, Calculation of electrical resistivity produced by dislocations and grain boundaries in metals, J. Phys. Condens. Matter. 6 (1994) 873–886. https://doi.org/10.1088/0953-8984/6/4/007.

[82] M. Kaveh, N. Wiser, Correlation between electron-dislocation scattering and electron-impurity scattering in metals, J. Phys. F Met. Phys. 11 (1981) 1749–1763. https://doi.org/10.1088/0305-4608/11/9/004.

[83] M. Kaveh, N. Wiser, Electrical resistivity of dislocations in metals, J. Phys. F Met. Phys. 13 (1983) 953–961. https://doi.org/10.1088/0305-4608/13/5/009.

[84] F.H. Featherston, J.R. Neighbours, Elastic constants of tantalum, tungsten, and molybdenum, Phys. Rev. 130 (1963) 1324–1333. https://doi.org/10.1103/PhysRev.130.1324.

[85] D.I. Bolef, J. De Klerk, Elastic Constants of Single-Crystal Mo and W between 77° and 500°K, J. Appl. Phys. 33 (1962) 2311–2314. https://doi.org/10.1063/1.1728952.

[86] R. Lowrie, A.M. Gonas, Single-Crystal Elastic Properties of Tungsten from 24° to 1800°C, J. Appl. Phys. 38 (1967) 4505–4509. https://doi.org/10.1063/1.1709158.

[87] D. Papadakis, S. Dellis, K. Mergia, V. Chatzikos, D. Terentyev, G. Bonny, A. Dubinko, W. Van Renterghem, M. Konstantinovic and S. Messoloras, The competing effects of temperature and neutron irradiation on the microstructure and mechanical properties of ITER grade tungsten, Fusion Engineering and Design 168 (2021) 112608, https://doi.org/10.1016/j.fusengdes.2021.112608.

[88] W. D. Nix and H. Gao, Indentation size effects in crystalline materials: A law for strain gradient plasticity, J. Mech. Phys. Solids 46 (1998) 411–25. https://doi.org/10.1016/S0022-5096(97)00086-0.

[89] S.J. Zinkle, Y. Matsukawa, Observation and analysis of defect cluster production and interactions with dislocations, J. Nucl. Mater. 329–333 (2004) 88–96. https://doi.org/10.1016/j.jnucmat.2004.04.298.

[90] D. Tabor, The physical meaning of indentation and scratch hardness, Br. J. Appl. Phys. 7 (1956) 159–166. https://doi.org/10.1088/0508-3443/7/5/301.

[91] D. Tabor, "The Hardness of Metals," Clarendon Press, Oxford, 1951

[92] J.T. Busby, M.C. Hash, G.S. Was, The relationship between hardness and yield stress in irradiated austenitic and ferritic steels, J. Nucl. Mater. 336 (2005) 267–278. https://doi.org/10.1016/j.jnucmat.2004.09.024.

[93] R.E. Stoller, S.J. Zinkle, On the relationship between uniaxial yield strength and resolved shear stress in polycrystalline materials, J. Nucl. Mater. 283–287 (2000) 349–352. https://doi.org/10.1016/S0022-3115(00)00378-0.